Topics in Catalysis (2020) 63:700–713
https://doi.org/10.1007/s11244-020-01297-w

ORIGINAL PAPER

Effect of Tin in the Bulk of Platinum–Tin Alloys for Ethane Dehydrogenation

Jinwoong Nam[1] · **Fuat E. Celik**[1]

Published online: 26 June 2020

Abstract

Catalytic ethane dehydrogenation was studied with density functional theory (DFT) calculations to investigate the differing role of Sn in the bulk and surface of PtSn alloys on the activity, selectivity, and stability of the catalyst. Pristine Pt(111), a surface alloy of Pt_3Sn/Pt(111) and a bulk alloy of Pt_3Sn(111) were compared. Binding energies of adsorbates were weakened by Sn on both alloys. With few changes for binding geometries of adsorbates, the change in binding energies was mainly attributed to the changes in the electronic interaction due to the strain effect and/or the ligand effect from *d*-band theory on the alloys. Especially, the combination of ligand and strain effects on the bulk alloy made the binding energies of adsorbates generally weaker than on Pt but stronger than on the surface alloy. In the successive dehydrogenation of C_2H_x species, the activity was expected in the order of $Pt > Pt_3Sn > Pt_3Sn/Pt$ by comparing the activation energies for ethene formation. The selectivity toward ethene was predicted using two descriptors from which the best selectivity was expected on Pt_3Sn/Pt. Sn in the bulk made the gap between the barriers for ethene desorption and further dehydrogenation comparable, whereas ethene desorption was much more favorable on Pt_3Sn/Pt. The preference for ethene formation from ethyl was also weakened on Pt_3Sn. Therefore, despite the higher Sn composition, worse selectivity was predicted for Sn-rich bulk alloy than the surface alloy, followed by Pt.

Keywords Ethane dehydrogenation · Density functional theory · PtSn alloys · Ethene · Selectivity · Coke

1 Introduction

Light alkane dehydrogenation has been of great interest to many engineers and scientists as light alkanes are abundant and have relatively low value whereas corresponding light alkenes are valuable as precursors for various polymers. Recently, it receives much more attention because the shale gas boom in North America involving the development of technology for its extraction and transportation has enabled economic production of a large amount of the natural gas feedstocks from shale gas [1–4].

For light alkane dehydrogenation, there are several processes including steam cracking, catalytic oxidative dehydrogenation, and catalytic dehydrogenation [5–7]. Steam crackers require hydrocarbon feedstocks such as naphtha and natural gas liquids diluted with steam at very high temperatures (1000−1200 K) in order to produce light olefins [8]. This is the well-established and most commercialized process for ethene production, though production of target olefins with high selectivity from C_4+ feed stocks is challenging. Frequent decoking operations are inevitable because the reaction suffers from significant coke deposition on the reactor walls due to the very high reaction temperatures, leading to inefficient reactor operation. Coke formation is limited by the addition of excess steam, at additional energy penalty. Therefore, these disadvantages along with low-cost gas feedstocks from shale gas have given rise to the necessity for energy-efficient and selective alternative processes using light alkanes. Catalytic dehydrogenation could be one of the potential alternatives given less harsh reaction conditions, where lower temperature (800−1000 K) is required for the reaction [9]. This process is also expected to be selective

Electronic supplementary material The online version of this article (https://doi.org/10.1007/s11244-020-01297-w) contains supplementary material, which is available to authorized users.

✉ Fuat E. Celik
fuat.celik@rutgers.edu

[1] Department of Chemical and Biochemical Engineering, Rutgers, The State University of New Jersey, 98 Brett Road, Piscataway, NJ 08854, USA

toward the targeted olefin product as an on-purpose technology. However, coke deposition on catalyst active sites leading to catalyst deactivation is still a significant problem for this process due to the elevated reaction temperature. Much effort has contributed to reducing coke formation while retaining competitive activity and selectivity of the catalyst, including changing catalyst composition and reaction conditions.

Supported platinum alloys have been widely used as catalysts for catalytic dehydrogenation. It has been shown that alloying Pt with other elements (e.g. Sn, Ga, In) shows superior overall performance in terms of activity, selectivity and stability compared to pristine Pt [10–14]. Tin has shown significant promise, so PtSn alloys are the most investigated both experimentally and computationally [11, 15–20].

PtSn alloys have been synthesized by impregnation of Pt and Sn using organometallic precursors on the support material followed by reduction, or by evaporating Sn of specific ratio onto Pt surface and annealing at high temperature (800–1000 K) afterward [10, 11, 21–23]. These catalysts were characterized by numerous techniques including transmission electron microscopy (TEM), inductively coupled plasma-atomic emission spectrometry (ICP-AES), energy-dispersive X-ray spectroscopy (EDS), where the composition and crystalline structure were reported [22, 24]. It has been reported for ethane dehydrogenation in that the activity of supported PtSn alloy catalysts increased with Sn addition for Sn/Pt ratio up to 0.3 and decreased above a ratio of 0.3. The selectivity toward ethene monotonically increased with adding Sn and reached almost 100% for Sn/Pt = 0.6 and above. Coke accumulation was significantly decreased with increasing Sn addition up to a Sn/Pt ratio of 0.3. Also, the experiment for hydrogen addition to the feed stream showed that hydrogen co-feeding up to a certain ratio reduced the amount of coke deposition on both Pt and PtSn alloy but the effect was larger on the latter [10, 11].

Many computational studies with density functional theory (DFT) have also been performed for dehydrogenation of various light alkanes including ethane and propane. PtSn alloys were modeled with various compositions and compared to pure Pt surfaces, including substitutional surface alloys (Pt_3Sn/Pt, Pt_2Sn/Pt, PtSn/Pt), bulk alloys (Pt_3Sn, Pt_2Sn, $PtSn_2$), as well as variations in exposed Miller index planes ((100), (111), (211)) [15–17, 25–28]. It has been reported that substituting Pt with Sn weakens the binding energies of hydrocarbon adsorbates due to a combination of the electronic effect and the geometric effect [17, 25, 29, 30]. This results in a weak adsorption energy for the product (e.g. ethene, propene) on alloy surfaces making desorption of the olefin easier while also disfavoring further dehydrogenation of the product, which could be a possible coke formation path. This is expected to lead to better selectivity and stability than pristine Pt. Generally, as the ratio of Sn/Pt increases, the difference between the energy barrier for olefin deep dehydrogenation and the desorption energy for the olefin product becomes larger due to increasing electronic and geometric effects [15, 25]. In this context, the experimental result for the improvement of selectivity and stability with increasing the ratio of Sn/Pt can be understood. The effect of hydrogen co-feeding on Pt and PtSn alloys for ethane dehydrogenation was also studied with DFT in terms of the competition for adsorption between co-fed hydrogen and ethene, where hydrogen outcompetes with ethene [25, 31].

In this study, we have calculated the complete reaction network from ethane to all dehydrogenated and C–C bond cleaved derivatives, including ethene, and compared the reaction energies and activation energy barriers for all the elementary reaction steps using DFT. We compare the pure Pt(111) surface to the surface alloy of Pt_3Sn/Pt(111) and the bulk alloy of Pt_3Sn(111) for potential energy surfaces, predict selectivity toward ethene, and provide insight into the mechanism of coke formation when the presence or absence of tin in the bulk. We discuss the impact of surface segregation of tin in the context of lattice strain and ligand effects, and distinguish activity and selectivity trends in tin-rich and tin-depleted bulk compositions for alloys.

2 Methods

Periodic, self-consistent, and spin-polarized DFT calculations were performed using the Vienna Ab initio Simulation Package (VASP) code [32, 33] within the generalized gradient approximation (GGA-PW91) [34] using projector-augmented wave (PAW) [35, 36] potentials. The single-electron wave functions were expanded using plane waves with an energy cutoff of 400 eV. All metal slabs were based on the (111) surface of fcc structure and modeled by a (2 × 2) surface unit cell with four atomic layers for a total of 16 metal atoms (Pt or Sn). For a (2 × 2) surface unit cell, all adsorbates were modeled at a coverage of 1/4 monolayer (ML). A larger surface unit cell size of (3 × 3) was tested for two adsorbates, methyl and ethyl, to simulate 1/9 ML coverage, to check for periodic image interaction effects, but these effects were small (< 0.05 eV) and were consistent between adsorbates of different sizes (e.g. 0.02 eV difference between ethyl and methyl adsorbates).

To generate the surface substitutional alloy, surface Pt atoms were substituted by Sn and the surface structure was reoptimized by relaxation. Substituting one Pt atom by Sn in the surface layer gives 1/4 ML Sn coverage. To construct the bulk alloy, bulk Pt atoms, as well as surface ones, were replaced with Sn atoms making the bulk composition of 1/4 Sn and the surface coverage of 1/4 ML Sn, followed by structure relaxation. The lattice constants of Pt and Pt_3Sn were calculated to be 3.99 Å and 4.07 Å, respectively, in

good agreement with experimental values of 3.92 Å and 4.00 Å [37, 38]. A vacuum layer of 12 Å was used to separate any two successive slabs in the *z*-direction (normal to the surface), and a dipole correction was applied and the electrostatic potential was adjusted to ensure that interaction between the surface slab and its periodic images was negligible [39]. The Brillouin zone was sampled using a (6×6×1) Gamma-centered Monkhorst–Pack k-point mesh [40] following a convergence test for adsorbate binding energies with respect to sampling mesh size. The bottom two layers of each metal slab were fixed in their bulk positions while the top two layers were allowed to relax in all calculations. Binding energy is defined as $BE = E_{ads} - E_{slab} - E_{gas}$, where E_{ads}, E_{slab}, E_{gas} are the total energies calculated for the slab with the adsorbate on it, the clean slab, and the adsorbate in the gas phase, respectively. The addition of a single adsorbate molecule to a metal slab with a (2×2) surface until cell corresponds to ¼ ML adsorbate coverage. The climbing image nudged elastic band (CINEB) method [41] was used to calculate transition state and activation energy barriers. All transition states were verified by identifying a single imaginary frequency along the reaction coordinate. All calculated energies were extrapolated to 0 K without zero point energy corrections. Zero point energy correction were tested for four adsorbates and two reaction steps (Online Resource 8) and found to be nearly identical across all three surfaces. Entropic contributions to surface reactions are expected to be small, but could be more significant for adsorption/desorption steps. This was tested for ethylene, and $\Delta S_{adsorption}$ on Pt(111), Pt_3Sn/Pt(111), and Pt_3Sn(111) was found to be invariant across the three surfaces (-0.00180 eV K^{-1} at 298 K).

3 Results and Discussion

3.1 Model Pt_3Sn/Pt(111) and Pt_3Sn(111) Surfaces

In the current study, two alloy models of Pt_3Sn/Pt(111) and Pt_3Sn(111) were established to study the effect of Sn both in PtSn bulk and in the surface as described in Table 1. Within a (2 × 2) unit cell, they both have the same 1/4 ML surface coverage of Sn by the replacement of one Pt atom.

One of the most important differences for two alloys is the existence of Sn atoms in bulk such that Pt_3Sn/Pt does not have Sn atoms in bulk while Pt_3Sn has 1/4 Sn bulk composition. The surface segregation energy of Sn in Pt_3Sn was calculated as -0.99 eV by $E_{Sn,seg} = E_{Sn\_1st} - E_{Sn\_2nd}$, where E_{Sn_1st}, E_{Sn_2nd} are the total energies of Pt_3Sn(111) slab with one Sn atom segregated on the surface layer, and on the second layer, respectively, within (6×6) unit cell [42]. Negative segregation energy with this equation implies that Sn prefers

Table 1 Structure of Pt(111) and two alloy models for this study

	Pt(111)	Pt_3Sn/Pt(111)	Pt_3Sn(111)
Top view	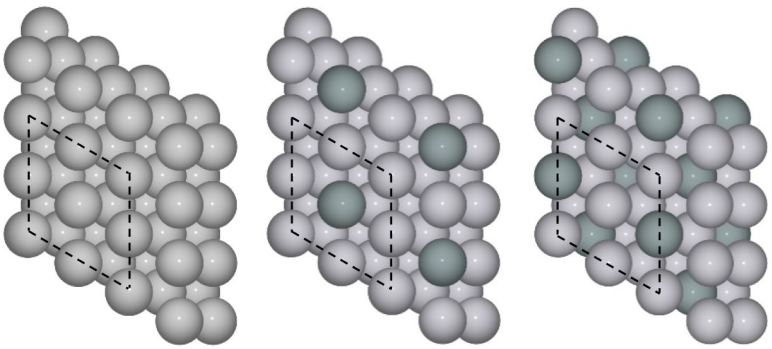		
Side view	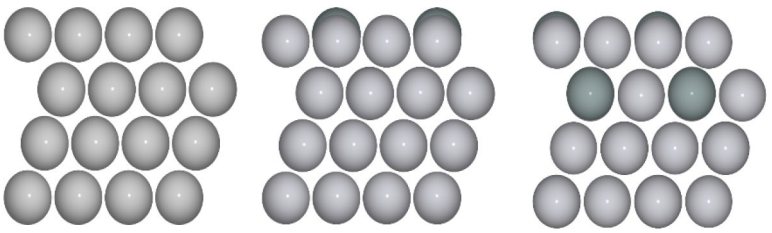		
Sn surface coverage	0 ML	1/4 ML	1/4 ML
Bulk composition	0 Sn	0 Sn	1/4 Sn
Lattice constant (Å)	3.99	3.99	4.07

Gray and green spheres denote Pt and Sn, respectively

Dashed lines indicate the unit cell used in the calculations

to stay on the surface rather than on the second layer. Pt_3Sn/Pt represents a totally segregated structure where all the tin has moved to the surface from the bulk. This represents one extreme for Sn depletion in the bulk. On the other hand, the Pt_3Sn model describes an evenly distributed bulk alloy with a uniform composition of Sn in both bulk and surface, which is the opposite extreme in terms of Sn segregation.

The other important difference between these two models is for the lattice constant. The fcc structure of Pt_3Sn/Pt is basically the same as fcc Pt bulk but decorated with Sn atoms only on the surface layer so its lattice constant remains the same as fcc Pt. Therefore, Pt_3Sn/Pt model is geometrically identical to Pt model in the bulk. In contrast, the lattice constant of fcc Pt_3Sn should be expanded relative to fcc Pt because Pt_3Sn includes larger Sn atoms in the bulk as well as in the surface layer. This leads to the larger calculated lattice constant of fcc Pt_3Sn (4.07 Å) than fcc Pt (3.99 Å). Therefore, in addition to the electronic effect from the Sn atoms, the tensile strain on the surface of Pt_3Sn could affect the interaction with adsorbates, as explored in subsequent sections.

The two alloy models can be thought to represent two different types of alloy particles that may be present in a real catalyst. The surface alloy represents a particle that has undergone significant surface segregation, where the bulk has been fully depleted of tin. The bulk alloy represents a particle where no surface segregation has taken place, and the tin distribution is homogeneous. By keeping the surface composition constant, the effect of the bulk composition on surface properties can be compared between the two extremes.

3.2 Binding of H & CH_x Species

The investigation of binding site preferences and energies for hydrogen and CH_x species (x = 0 to 4) on Pt and PtSn alloys was performed as summarized in Fig. 1 and Table 2. Except for a few minor differences, all binding site preferences and binding energies were in agreement with previously reported results [16, 25, 26, 29, 30, 43, 44].

In Fig. 1, the hydrogen atom is preferably adsorbed on a three-fold hollow site only consisting of three Pt atoms over all surfaces. It is noted that the best binding site for hydrogen on Pt, the fcc site, remained the same on the surface alloy but changes to hcp_Sn site on the bulk alloy. A detailed discussion on the binding of hydrogen can be found in Online Resource 1. H_2 only interacted weakly with the surfaces (−0.02 eV).

For CH_x species, we previously reported that sp^3-hybridized carbon structure is preferred for binding geometries of CH_x species on Pt or Pt based alloys with the exception of atomic carbon [25, 30]. Also, on PtSn alloys, adsorbates of CH_x species are more favorably adsorbed with ensembles only consisting of Pt atoms rather than Sn atoms. As

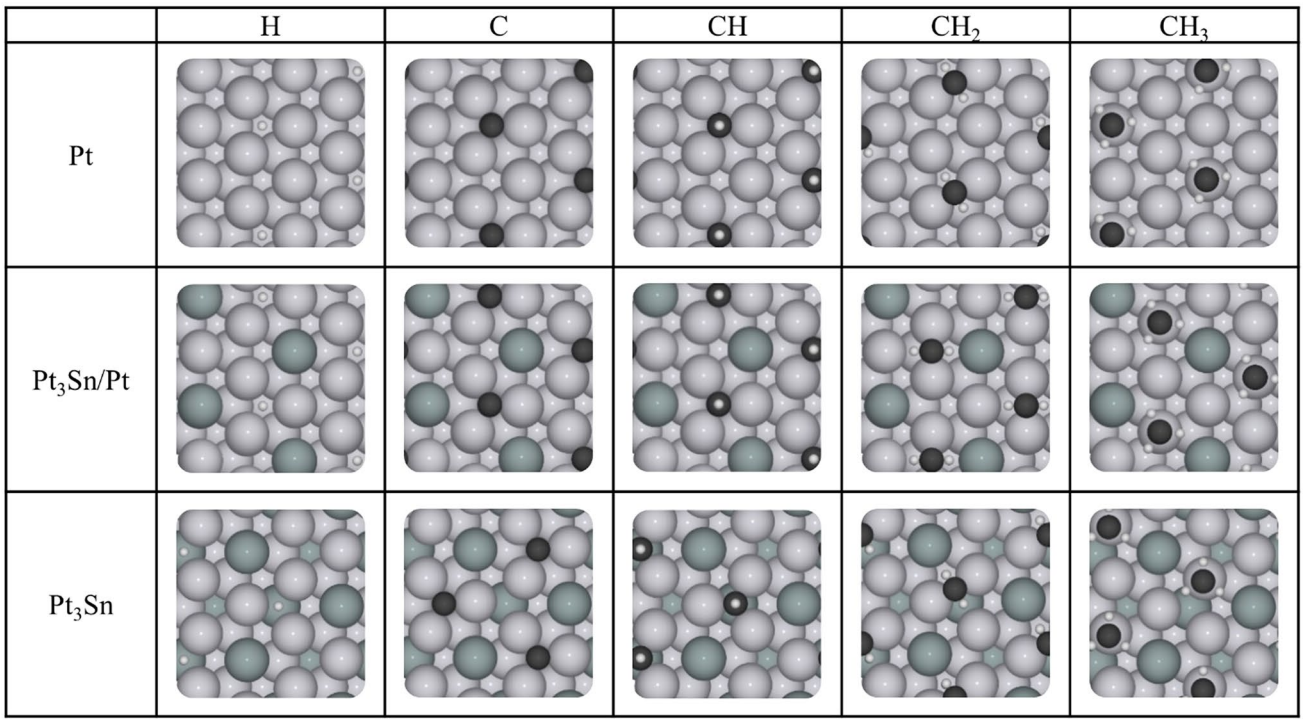

Fig. 1 Best binding sites for H and CH_x species on Pt, Pt_3Sn/Pt, and Pt_3Sn. Pt, Sn, C, and H atoms are gray, green, black, and white spheres, respectively. This color notation is used throughout the paper

Table 2 Best binding sites, binding energies, and the coordination numbers with Pt for H, H_2 and CH_x species on all studied surfaces

Adsorbate	Name	Pt			Pt_3Sn/Pt			Pt_3Sn		
		Site	BE[a]	CN_{Pt}[b]	Site	BE[a]	CN_{Pt}[b]	Site	BE[a]	CN_{Pt}[b]
H	Hydrogen	fcc	−2.72*	3	fcc	−2.67*	3	hcp_Sn[d]	−2.72*	3
H_2	Dihydrogen	–[c]	−0.02	0	–[c]	−0.02	0	–[c]	−0.02	0
C	Carbon	fcc	−6.97	3	fcc	−6.29	3	fcc_Sn[d]	−6.16	3
CH	Methylidyne	fcc	−6.70	3	fcc	−6.09	3	hcp_Sn[d]	−6.12	3
CH_2	Methylene	brg	−4.14	2	brg	−3.80	2	brg	−3.96	2
CH_3	Methyl	top	−2.07	1	top	−1.86	1	top	−1.96	1
CH_4	Methane	–[c]	−0.03	0	–[c]	−0.03	0	–[c]	−0.04	0

[a]BE is the binding energy in eV

[b]CN_{Pt} is the coordination number of carbon for CH_x species or H to Pt at the binding site

[c]H_2 and CH_4 interacts weakly without any site preferences

[d]hcp_Sn and fcc_Sn mean an hcp site over Sn atom on the second layer and an fcc site over Sn atom on the third layer, respectively

*Binding energy of hydrogen was adjusted from the raw calculations. See Online Resource 1 for details. Binding energy of hydrogen relative to 1/2 H_2 is −0.45, −0.39, and −0.44 eV on Pt, Pt_3Sn/Pt, and Pt_3Sn, respectively

depicted in Fig. 1, our calculations show consistent results with previous reports on Pt, Pt_3Sn/Pt, and Pt_3Sn. That is, while no H–Sn or C–Sn bond is preferred the carbon atom of CH_x species tends to make a total of four bonds with hydrogen and Pt atoms constructing tetravalent carbon structure on the surfaces. The only exception is atomic carbon with three C–Pt bonds which are the maximum coordination numbers for fcc (111). Methylidyne includes one C–H bond so it prefers to be adsorbed on a three-fold hollow site such as an fcc or an hcp site with three C–Pt bonds. The best binding site of methylidyne is different from each other surface, where an fcc site is preferred on Pt and Pt_3Sn/Pt while an hcp_Sn site (hcp site over Sn) is preferred on Pt_3Sn. Nevertheless, it should be noted that they are still all threefold hollow sites. Methyl is noteworthy in that it is bound atop a Pt atom on Pt and Pt_3Sn/Pt but on slightly off-position from atop a Pt atom on Pt_3Sn. Unlike the CH_x species, methane is fully coordinated with hydrogen atoms, so it only has weak interaction (binding energy of 0.03 or 0.04 eV) on all surfaces without any site preference, like H_2. While CH_x species basically prefers to bind to Pt atoms constructing four carbon bonds, no significant geometric change is observed with Sn addition in the surface and bulk. On both alloys, Pt ensembles consisting of three Pt atoms can be retained with 1/4 ML surface coverage of Sn, which offers almost the same site environment as pure Pt available to adsorbates. From this geometric point of view, a similar preference for binding sites of CH_x species on all studied surfaces is understandable. Only three-fold hollow sites on Pt_3Sn are different from those on the other two surfaces such that an hcp and an fcc site consisting of three Pt atoms are over Sn atom in the second layer and in the third layer, respectively. It may affect a shift in the best binding site of hydrogen and methylidyne on Pt_3Sn.

Binding energies of CH_x species on three surfaces are given with the number of C–Pt bonds in Table 2. Binding became stronger with an increasing number of C–Pt bonds on all surfaces. Ranging from methylidyne to methane, it was demonstrated in our previous calculations that one C–Pt bond strengthens the binding of adsorbate by roughly 2 eV on Pt and Pt_3Sn/Pt [25]. The results in Table 2 indicate a similar energy difference of about 2 eV per C–Pt bond on the bulk alloy Pt_3Sn surface. Consequently, the number of C–Pt bonds can serve as one of the qualitative indicators to measure binding energies of CH_x species on the studied surfaces. For carbon and methylidyne, which both have the same number of C–Pt bonds, calculated binding energies showed that the former is bound stronger than the latter by 0.04–0.27 eV depending on the surface. It is also supported by the fact that the maximum distances of C–Pt bonds for carbon/methylidyne on Pt, Pt_3Sn/Pt, and Pt_3Sn are 1.924/2.007 Å, 1.956/2.022 Å, and 1.975/2.045 Å, respectively, which always displays shorter C–Pt bond lengths for atomic carbon than for methylidyne on each surface. It may imply that the frustrated fourth C–Pt bond for carbon could be replaced by reinforced binding on the surface.

The effect of Sn can be found in Table 2 by comparing the binding energies of CH_x species on Pt to those on two PtSn alloys. Binding energies were always stronger on Pt than on either alloy. For example, atomic carbon binds to Pt(111) with a binding energy of −6.97 eV but to Pt_3Sn/Pt and Pt_3Sn surfaces with binding energies of −6.29 and −6.16 eV, respectively. This weakening of the binding energy generally increased with the number of C–Pt bonds. Methylidyne, which has three C–Pt bonds, binds to pure Pt with the

binding energy of −6.70 eV and to Pt_3Sn/Pt and Pt_3Sn with binding energies of −6.09 and −6.12 eV, respectively, for a weakened binding energy of approximately 0.6 eV on the alloys. For methylene and methyl, which have two and one C–Pt bonds respectively, the difference of binding energies between Pt and Pt_3Sn/Pt was 0.34 and 0.21 eV, and between Pt and Pt_3Sn was 0.18 and 0.11 eV respectively. It should be noted that increasing the total tin content in the alloy did not mean a weaker binding energy. Previous comparisons of substitutional surface alloys with different tin content reported that alloying with more Sn in the surface layer corresponds to weaker binding energies due to the greater electronic effect in combination with changes in geometric binding sites [15, 25]. In the present study, however, increasing the Sn content in the bulk was not associated with weaker binding energies of CH_x species compared to the surface alloy. The binding energies on Pt_3Sn were stronger than on Pt_3Sn/Pt for methylidyne, methylene, and methyl. This suggests that Sn in the bulk does not necessarily reinforce the electronic effect on the surface, or another factor aside from the electronic effect may affect binding energies of adsorbates on Pt_3Sn. This is discussed further in Sect. 3.3.

Another important impact of adsorbates is the potential to change the segregation energy. In the previous section, the segregation energy for Sn atoms in a clean surface (no adsorbates) was −0.99 eV. This calculation was repeated for a surface with 1/4 ML of hydrogen and carbon atoms. In the case of hydrogen, the segregation energy was nearly half (−0.51 eV) the clean surface. The change in segregation energy dramatically increased with carbon adsorbed where the calculated segregation energy was only −0.02 eV. The addition of hydrogen or carbon to the surface clearly made surface segregation less likely than in the case of the clean surface. This highlights the importance in comparing the two alloy models used in this paper, as the distribution of Sn atoms in a nanoparticle may vary with reaction conditions.

3.3 Binding of C_2H_x Species

Binding geometries and energies for C_2H_x species (x = 0 to 6) are given in Fig. 2 and Table 3. For all surfaces, a tetrahedral structure around each carbon was generally preferred, in agreement with the findings for CH_x species and in previous reports [45, 46].

Isoelectronic adsorbates such as CH_x and CH_3CH_{x-1} are expected to have similar binding geometries [25, 44]. For example, in Fig. 2, the carbon involved in binding in ethyl favorably binds to atop Pt on all surfaces, which is consistent with the binding geometry of methyl. Ethylidene prefers to bind to a Pt bridge site as methylene does and ethylidyne is highly favorable to bind to a threefold Pt site like methylidyne. For ethylidyne, a shift in preferred binding site from an fcc site to an hcp_Sn site on Pt_3Sn was found as seen for hydrogen and methylidyne. For C_2H_x adsorbates other than CH_3CH_{x-1} species, both carbons in the adsorbates participate in binding on the surface. Ethene favors binding to two adjacent Pt top sites forming two σ metal–carbon bonds. Vinyl preferably binds to a Pt top-brg site but with slightly different geometries depending on the surface. The best binding geometry is top-brg over an fcc site on Pt but over an hcp site on Pt_3Sn/Pt and Pt_3Sn. Similarly, vinylidene prefers to bind to top-fcc on Pt and Pt_3Sn/Pt but prefers a top-hcp_Sn site on Pt_3Sn. Acetylene binds to brg-brg site over an fcc site on Pt and Pt_3Sn/Pt, but over an hcp_Sn site on Pt_3Sn. The binding preference of acetylidene is different from each surface such that brg-fcc, top-fcc, and top-brg are favored over Pt, Pt_3Sn/Pt, and Pt_3Sn, respectively. Dicarbon binds to fcc-hcp site on all surfaces and inevitably has one C–Sn bond on the alloys. Structural changes of C_2H_x species on the surface along with the binding site preference were found. A detailed discussion can be found in Online Resource 2.

The binding energies of C_2H_x species on Pt, Pt_3Sn/Pt, and Pt_3Sn presented in Table 3 can be interpreted in terms of the *d*-band model of transition metals. Since it was first developed by Hammer and Nørskov in 1995 [47, 48], *d*-band theory has been successfully employed to understand the interaction (e.g. adsorption/desorption) between surface metals and adsorbates. This model argues that the *d*-bands of surface metal strongly correlate with binding energies of the adsorbates. As a descriptor of the *d*-band, the first moment corresponding to the average energy of the band with respect to Fermi level has been widely used, which is called the *d*-band center. For the surface consisting of late transition metals such as Pt, previous studies have shown that the binding energies of adsorbates qualitatively increase with the position of the *d*-band center relative to Fermi level because the higher *d*-band center of the metals leads to less filled anti-bonding states of metal-adsorbate and vice versa [15, 49].

The density of states (DOS) projected onto the *d*-orbitals of surface Pt atom and its *d*-band center were investigated as shown in Fig. 3. Calculated energies of *d*-band centers were −1.95 eV for Pt, −2.10 eV for Pt_3Sn/Pt, and −2.02 eV for Pt_3Sn, which is consistent with previous reports [15, 50]. Given the fact that all the surfaces have the same structure of fcc(111), the major two factors resulting in the change of *d*-band center positions for the alloys relative to pristine Pt are the ligand effect and the strain effect. The ligand effect is caused by the change in electronic interactions mainly due to introducing a new element (i.e. Sn). By alloying Pt with Sn, *d*-bands of Pt atoms become broadened due to bonding interaction with Sn atoms, which is followed by its downshift for charge conservation. The lower energy of the *d*-band center for Pt_3Sn/Pt than for Pt is attributed to this effect. On the other hand, the strain effect comes from

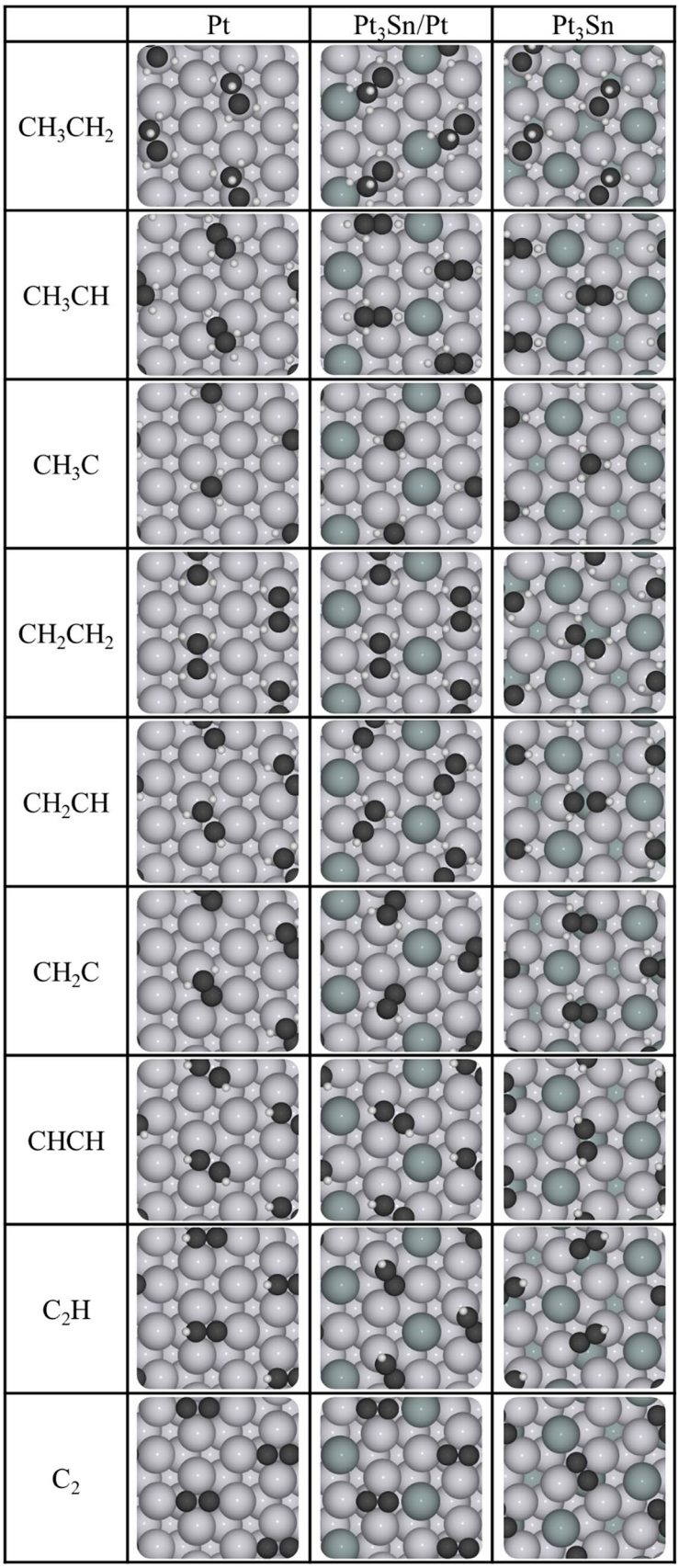

Fig. 2 Best binding sites for C_2H_x species on Pt, Pt_3Sn/Pt, and Pt_3Sn

Table 3 Best binding sites, binding energies for C_2H_x species on all studied surfaces

Adsorbate	Name	Pt		Pt_3Sn/Pt		Pt_3Sn	
		Site	BE[a]	Site	BE[a]	Site	BE[a]
CH_3CH_3	ethane	–[b]	− 0.07	–[b]	− 0.06	–[b]	− 0.07
CH_3CH_2	ethyl	top	− 1.90	top	− 1.65	top	− 1.77
CH_3CH	ethylidene	brg	− 3.86	brg	− 3.49	brg	− 3.62
CH_3C	ethylidyne	fcc	− 5.93	fcc	− 5.30	hcp_Sn[c]	− 5.35
CH_2CH_2	ethene	top-top	− 1.03	top-top	− 0.65	top-top	− 0.77
CH_2CH	vinyl	top-brg	− 3.12	top-brg	− 2.64	top-brg	− 2.92
CH_2C	vinylidene	top-fcc	− 4.36	top-fcc	− 3.73	top-hcp_Sn[c]	− 3.92
CHCH	acetylene	brg-brg	− 2.21	brg-brg	− 1.60	brg-brg	− 1.91
CHC	acetylidene	brg-fcc	− 4.55	top-fcc	− 3.93	top-brg	− 4.37
C_2	dicarbon	fcc-hcp	− 5.95	fcc-hcp	− 5.21	fcc-hcp_Sn[c]	− 5.63

[a]BE is the binding energy in eV

[b]CH_3CH_3 interacts weakly without any site preferences

[c]hcp_Sn indicates hcp site over Sn atom on the second layer

a geometrical change of the surface structure such as lattice constant expansion/contraction. According to the theory, tensile strain induced by the elongated lattice constant leads to less overlap in *d*-orbitals between surface atoms leading to sharpening of the *d*-bands. To conserve total charge in the *d*-orbitals, it is necessary to shift the entire *d*-band upward [51]. This is the case for the bulk alloy which has a larger lattice constant than Pt or the surface alloy. The difference in bulk composition for the Pt_3Sn alloy also causes a concurrent ligand effect which lowers the *d*-band center. Therefore, the competition between the two effects determines the position of the *d*-band center for Pt_3Sn.

An investigation which separates the ligand effect from the strain effect and their influence on DOS of the surfaces was carried out using surface with hypothetical lattice constants and are included in Online Resource 3.

Higher *d*-band centers lead to stronger binding energies by giving rise to less-filled anti-bonding states of the metal-adsorbate interaction and vice versa. In this context, the binding energies of C_2H_x species on Pt, Pt_3Sn/Pt and Pt_3Sn presented in Table 3 are generally consistent with the *d*-band model. In Fig. 3, the *d*-band center position for Pt is the highest among three surfaces and binding energies of all adsorbates are also the strongest accordingly (Fig. S1). For Pt_3Sn/Pt, the energy of the *d*-band center is lowest due to a strong ligand effect, which leads to the weakest binding energies with the exception of carbon. For Pt_3Sn, both contributions from the strain and the ligand effect result in the intermediate position of *d*-band center and binding energies of adsorbates as well (Fig. S1).

Along with the study for DOS on the surfaces with hypothetical lattice constants, binding energies of C_xH_y species on these surfaces were calculated to investigate the relationship between *d*-band center position and binding energy of individual adsorbate. A detailed discussion can be found in Online Resource 3.

In conclusion, the strain and ligand effect from *d*-band theory gives great insights into the difference of binding energies for C_xH_y species between studied surfaces. Generally, it is consistent with the calculations for *d*-band centers of surface Pt atoms as shown in Figure S1. Since Sn causes broadening the *d*-band of surface Pt atoms without the strain effect for the surface alloy, it is downshifted from pure Pt. Higher energy for the *d*-band center of surface Pt atoms on the bulk alloy than the surface alloy is attributed to the *d*-band upshift caused by lattice constant expansion. The combination of upshift by strain effect and the downshift by ligand effect locates the *d*-band center position for Pt_3Sn, which is the intermediate among three models. From further investigation with hypothetical lattice constants, a noteworthy is that when Sn is promoted in the bulk, monotonic downshift of *d*-band center or decrease of binding energies for adsorbates is not observed. Instead, it unpredictably affects the *d*-band center or the binding energies of the adsorbates.

3.4 Hydrogen Coadsorption with C_xH_y Species

The effect of co-adsorbed hydrogen for binding energies of C_xH_y species was studied. While binding energies of all adsorbates were always reduced by co-adsorbed hydrogen due to repulsive interaction between adsorbates and hydrogen, binding geometries were changed only for a few adsorbates. Hydrogen relatively freely changed its preferred binding site in the presence of co-adsorbed C_xH_y species over all surfaces because of its small energy barrier for diffusion on the surface. On Pt, only acetylidene and ethylidene changed their best binding geometries with co-adsorbed hydrogen. Acetylidene preferred to bind to brg-fcc site on Pt without

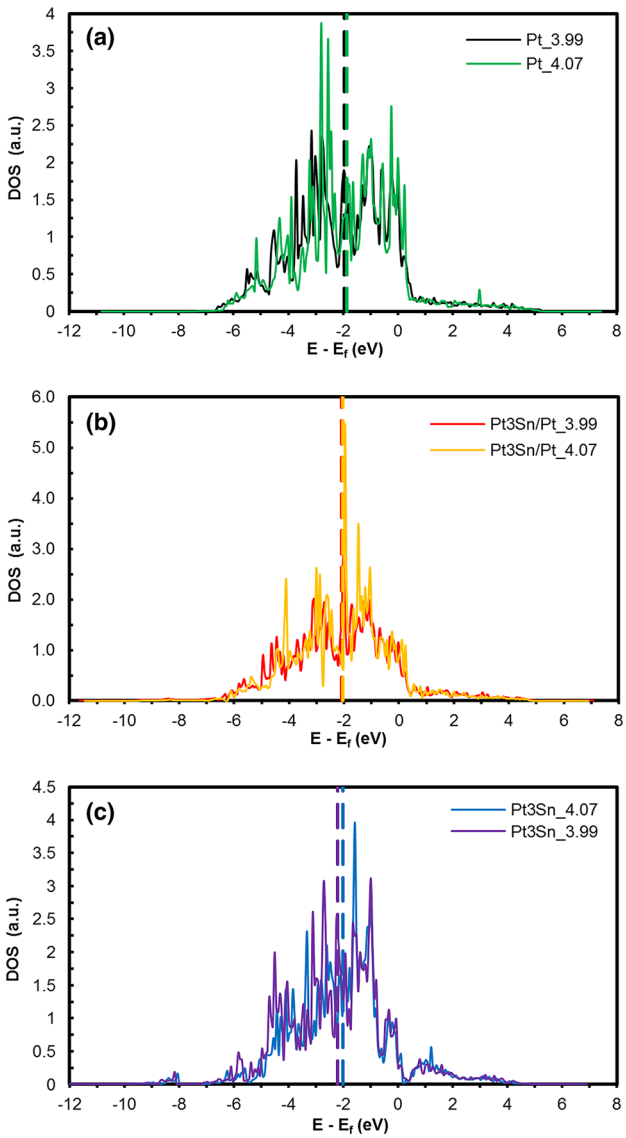

Fig. 3 Projected DOS onto *d*-orbitals of surface Pt atom on **a** Pt_3.99 and Pt_4.07, **b** Pt_3Sn/Pt_3.99 and Pt_3Sn/Pt_4.07, and **c** Pt_3Sn_4.07 and Pt_3Sn_3.99. Numbers marked after the surfaces indicate lattice constants in Å

hydrogen but changed to top-fcc site with co-adsorbed hydrogen. The carbon from ethylidene preferred to bind to a brg site both with and without hydrogen but they had quite different binding angles from each other. On Pt_3Sn/Pt, acetylidene, acetylene, ethylidene, and ethyl changed their favorable binding sites when hydrogen was co-adsorbed. The change for binding geometry of acetylidene accompanied the decrease of coordination number to Pt as from top-fcc to top-brg while the other three species kept the same binding site with the same coordination numbers to Pt but having different configurations. On Pt_3Sn, carbon and ethene were two adsorbates changing their best binding geometries with co-adsorbed hydrogen. Carbon experienced a three-fold hollow site shift from fcc_Sn to hcp_Sn and ethene bound to two different top–top sites depending on the existence of co-adsorbed hydrogen.

The decrease of binding energies for C_xH_y adsorbates by competition from co-adsorbed hydrogen is very dependent on surfaces and adsorbates. On Pt, binding energies of C_xH_y species were weakened by 0.09–0.33 eV, methyl seeing the smallest impact due to its small size and acetylidene seeing the largest impact. The hydrogen coadsorption effect was similar on the alloys, but larger for some adsorbates. On Pt_3Sn/Pt, the maximum effect was a 0.42 eV weakening of the binding energy of dicarbon, and on Pt_3Sn, vinylidene experienced the largest effect of 0.44 eV. Ethylidene notably saw negligible effect on binding energy from hydrogen co-adsorption on Pt_3Sn, whereas hydrogen weakened the binding energy by 0.16 and 0.12 eV on Pt and Pt_3Sn/Pt respectively. This implies that ethylidene would be barely destabilized in the presence of hydrogen on the bulk alloy. Ethene is also an important adsorbate since its desorption always affects the selectivity of the entire reaction. The binding energy of ethene was reduced with co-adsorbed hydrogen by 0.23, 0.14, and 0.18 eV on Pt, Pt_3Sn/Pt, and Pt_3Sn, respectively. Since binding energy of ethene becomes weaker by the addition of hydrogen on the surfaces, desorption is expected to be more favored on hydrogen-rich conditions than hydrogen-free surfaces leading to better selectivity as observed in previous hydrogen co-feeding experiments [10, 11, 13, 52].

3.5 Activation Energy Barriers for C–H Bond-Breaking Steps

Successive dehydrogenation of ethane derivatives was studied on each surface with three different pathways depending on the C–H cleavage position as shown in Fig. 4. The three identified pathways progress via different intermediates, and are: the ethene pathway (ethyl → ethene → vinyl → vinylidene → acetylidene); the ethylidyne pathway (ethyl → ethylidene → ethylidyne → vinylidene → acetylidene); and the vinyl pathway (ethyl → ethylidene → vinyl → acetylene → acetylidene). Reaction and activation energies for all elementary reactions including C–H and C–C cleavage and ethylidene isomerization are summarized in Table 4 and Fig. 4. Images of initial, final and transition state structures for all elementary steps are given in Online Resources 4–7.

Most C–H cleavage steps were found to be endothermic with large activation energy barriers on all three surfaces. Reaction energies became more endothermic on the Pt_3Sn/Pt surface alloy relative to pure Pt(111), and activation energy barriers were larger as well. Dehydrogenation of ethyl to form ethylene was an exception, and was exothermic on all three surfaces with a small activation energy barrier. The

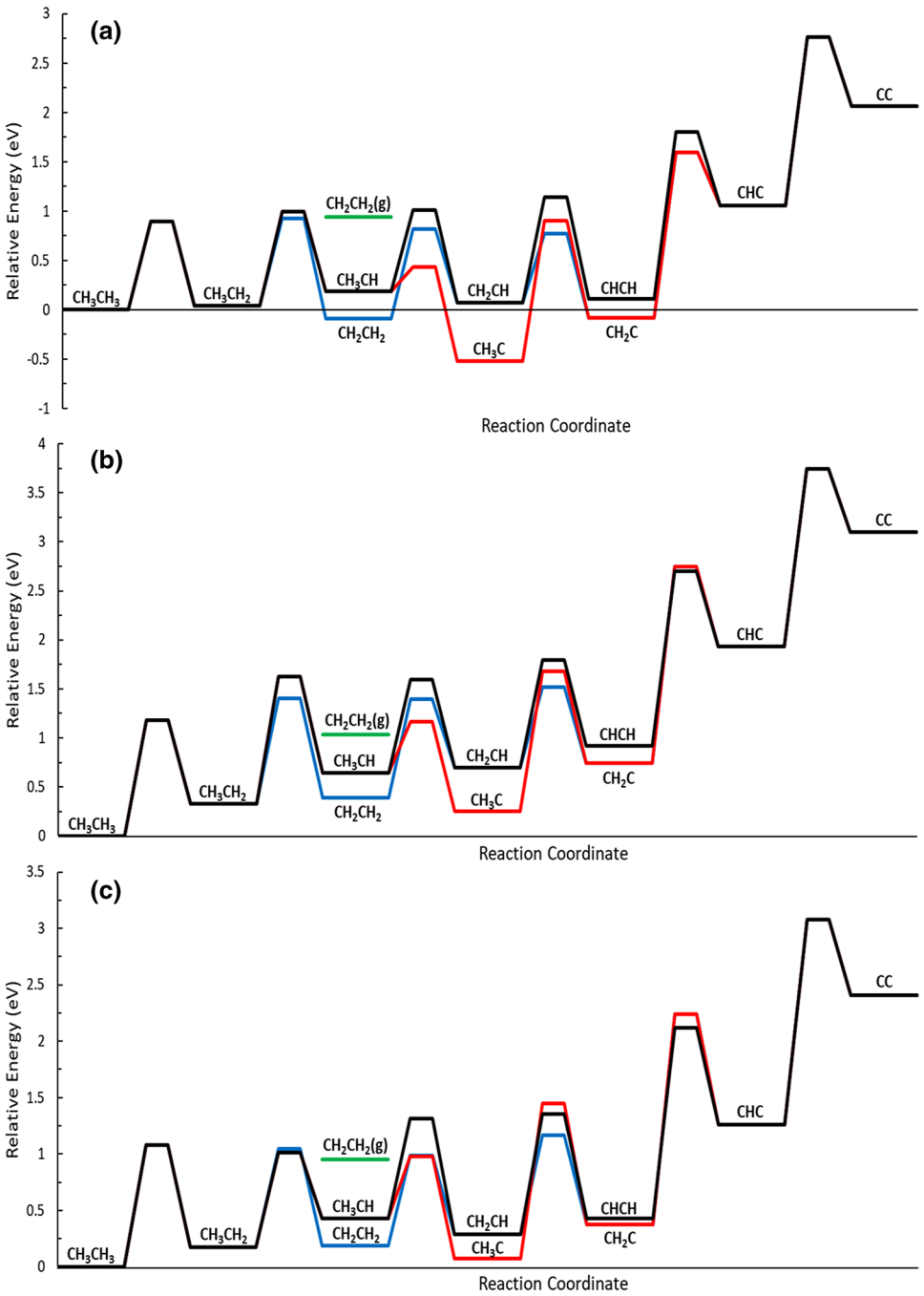

Fig. 4 Potential energy surfaces for successive dehydrogenation of C_2H_x species from ethane to dicarbon on **a** Pt, **b** Pt_3Sn/Pt, and **c** Pt_3Sn. All energies are relative to ethane on the surface. Gas phases are marked, and all other species are adsorbed on the surface. Detached hydrogens on the surfaces are omitted for clarity and all species are at infinite separation. Ethene pathway, ethylidyne pathway, and vinyl pathway are shown in blue, red, and black, respectively. Ethene desorption energy is shown in green

Pt_3Sn bulk alloy showed intermediate reaction energies and activation energy barriers for some, but not all reactions. For reactions 10, 11, 12, 15, and 16, the C–H cleavage step was actually more exothermic and thermodynamically more facile on the bulk alloy than on even pure platinum. Despite the high extent of tin substitution in the bulk alloy, the lattice expansion effect had a larger effect on reaction energy than the ligand effect for these reactions. Notably, the product state in each of these five elementary reactions involved species bound to top-brg and top-hollow sites (vinyl, vinylidene, acetylidene) while all other reactions had products that bound to other sites. The increased lattice spacing of the bulk alloy was closer to the optimal top-brg and top-hollow distances to accommodate the C–C bond in these species, making these product states more favorable (Fig. 2). This effect did not play a large role in the reaction energies for the other steps. Overall, the potential energy surface for bulk Pt_3Sn given in Fig. 4 appears to be intermediate between that of Pt and the surface alloy, but differs from both in the cases of these key intermediates. For this reason, the selectivity

Table 4 Reaction energies[a] and activation energies[b] for elementary reactions (in eV)

No	Step[c]	Pt		Pt_3Sn/Pt		Pt_3Sn	
		ΔE	E_a	ΔE	E_a	ΔE	E_a
1	$H_2+2^* \rightarrow 2H^*$	−0.88	0.03	−0.76	0.15	−0.85	0.09
2	$CH_4+2^* \rightarrow CH_3^*+H^*$	0.06	0.91	0.32	1.15	0.18	0.95
3	$CH_3^*+^* \rightarrow CH_2^*+H^*$	0.21	0.91	0.39	0.99	0.28	0.75
4	$CH_2^*+^* \rightarrow CH^*+H^*$	−0.50	0.29	−0.17	0.56	−0.09	0.60
5	$CH^*+^* \rightarrow C^*+H^*$	0.68	1.43	0.79	1.46	0.92	1.64
6	$CH_3CH_3+2^* \rightarrow CH_3CH_2^*+H^*$	0.04	0.90	0.33	1.18	0.17	1.08
7	$CH_3CH_2^*+^* \rightarrow CH_3CH^*+H^*$	0.14	0.95	0.32	1.30	0.26	0.84
8	$CH_3CH_2^*+^* \rightarrow CH_2CH_2^*+H^*$	−0.13	0.88	0.06	1.08	0.01	0.88
9	$CH_3CH^*+^* \rightarrow CH_3C^*+H^*$	−0.71	0.25	−0.39	0.52	−0.36	0.55
10	$CH_3CH^*+^* \rightarrow CH_2CH^*+H^*$	−0.11	0.83	0.05	0.95	−0.14	0.88
11	$CH_3C^*+^* \rightarrow CH_2C^*+H^*$	0.44	1.43	0.49	1.42	0.30	1.38
12	$CH_2CH_2^*+^* \rightarrow CH_2CH^*+H^*$	0.16	0.91	0.31	1.00	0.10	0.80
13	$CH_2CH^*+^* \rightarrow CH_2C^*+H^*$	−0.16	0.70	0.04	0.82	0.09	0.88
14	$CH_2CH^*+^* \rightarrow CHCH^*+H^*$	0.04	1.06	0.22	1.09	0.14	1.06
15	$CH_2C^*+^* \rightarrow CHC^*+H^*$	1.14	1.68	1.19	2.01	0.89	1.87
16	$CHCH^*+^* \rightarrow CHC^*+H^*$	0.94	1.69	1.01	1.78	0.83	1.69
17	$C_2H^*+^* \rightarrow C_2^*+H^*$	1.00	1.71	1.17	1.82	1.15	1.82
18	$CH_3CH_3+2^* \rightarrow CH_3^*+CH_3^*$	0.20	3.27	0.61	2.84	0.41	3.42
19	$CH_3CH_2^*+^* \rightarrow CH_3^*+CH_2^*$	0.37	1.90	0.68	1.95	0.52	1.68
20	$CH_3CH^*+^* \rightarrow CH_3^*+CH^*$	−0.28	1.30	0.19	1.52	0.17	1.52
21	$CH_3C^*+^* \rightarrow CH_3^*+C^*$	1.11	2.22	1.36	2.31	1.44	2.28
22	$CH_2CH_2^*+^* \rightarrow CH_2^*+CH_2^*$	0.71	2.26	1.00	2.07	0.79	2.25
23	$CH_2CH^*+^* \rightarrow CH_2^*+CH^*$	0.04	1.72	0.52	2.28	0.60	2.54
24	$CH_2C^*+^* \rightarrow CH_2^*+C^*$	0.88	2.32	1.27	2.36	1.43	2.67
25	$CHCH^*+^* \rightarrow CH^*+CH^*$	−0.49	1.37	0.13	2.46	0.37	2.78
26	$CHC^*+^* \rightarrow CH^*+C^*$	−0.76	1.24	−0.09	1.84	0.45	3.06
27	$C_2^*+^* \rightarrow C^*+C^*$	−1.08	1.25	−0.47	1.62	0.22	2.07
28	$CH_3CH^* \rightarrow CH_2CH_2^*$	−0.27	2.02	−0.26	2.07	−0.25	2.13

[a] ΔE is the energy of reaction at infinite separation

[b] E_a is the activation energy barrier for the reaction

[c] An asterisk with a species indicates a species bound to the surface; an asterisk alone denotes an empty site on the surface. The species without asterisk indicate weakly physisorbed species on the surface

and mechanism towards gaseous products versus coke formation on the bulk alloy may be expected to differ from that of the surface alloy.

The activity of these catalysts for ethane dehydrogenation can be described by the activation energy barriers to the formation of ethene along the ethene pathway. The barriers for the two steps in ethene formation, dehydrogenation of ethane to ethyl and subsequent dehydrogenation of ethyl to ethene, were 0.90 eV and 0.93 eV on Pt, 1.08 eV and 1.05 eV on Pt_3Sn, and 1.18 eV and 1.41 eV on Pt_3Sn/Pt. Intrinsic activity for ethene formation may therefore be expected to be highest for Pt and lowest for the surface alloy, especially with the significantly higher barrier for ethene formation.

In previous work, we defined a selectivity descriptor for ethane dehydrogenation by comparing the desorption of ethene, leading to the desirable product, to the dehydrogenation of ethene, leading to decomposition products and coke formation [30]. The descriptor, calculated from the activation energy for ethene dehydrogenation ($E_{a,CH_2CH_2 \rightarrow CH_2CH}$) and the desorption energy of ethene ($\Delta E_{des,CH_2CH_2}$) was used to predict selectivity trends among several substitutional surface alloy compositions [30].

$$\text{Selectivity descriptor} = E_{a,CH_2CH_2 \rightarrow CH_2CH} - \Delta E_{des,CH_2CH_2}$$

Smaller and more negative values of the selectivity descriptor indicate that it is easier to decompose ethene formed on the surface than to remove it, indicating poorer selectivity towards the desired product, and predicting greater coke formation. The selectivity descriptor is calculated as −0.12 eV on Pt indicating poor selectivity. On the surface alloy, the descriptor value is +0.36 eV, so selectivity

favors ethene formation. The bulk alloy has an intermediate value of 0.04 eV, which suggests poorer selectivity than on the surface alloy. These values were calculated without considering entropic contributions to $\Delta E_{\mathrm{des,CH_2CH_2}}$, though entropy of adsorption was found to be invariant across the surfaces, so adding $-T\Delta S$ at 298 K would raise all three values by 0.54 eV, or 1.48 eV at 900 K, and preserving the same trend.

Additionally, it should be noted while the ethene pathway is both kinetically and thermodynamically preferred to ethylidene or vinyl pathway for the dehydrogenation of ethyl on Pt_3Sn/Pt, this pathway is kinetically less favorable on Pt and Pt_3Sn as the energy barrier for ethene formation is comparable to the barrier for ethylidene formation as shown in Fig. 4. This leads to lower ethene selectivity on Pt and Pt_3Sn due to an expected increase in the reaction flux for ethylidene formation and further decomposition products. Comparing the reaction energies for these two major fluxes (ethyl dehydrogenation leading to ethene and to ethylidene) shows little difference between the three surfaces ($\Delta\Delta E = 0.25$–0.27 eV, Table 5). Comparing instead the activation energies of ethyl to ethylidene ($E_{\mathrm{a,CH_3CH_2\rightarrow CH_3CH}}$) and to ethene ($E_{\mathrm{a,CH_3CH_2\rightarrow CH_2CH_2}}$) shows that these pathways are comparable on Pt and the bulk alloy (+0.07 eV and −0.03 eV apart on each surface respectively), ethylidene formation is 0.22 eV more difficult on the surface alloy.

Both metrics for selectivity (Table 5) therefore show favorable intrinsic selectivity on Pt_3Sn/Pt, while selectivity on both Pt and the bulk alloy are expected to be poor, despite the significantly higher tin content in the bulk alloy This result suggests that particles that have significant tin migration to the surface and depletion of tin in the bulk are expected to be more selective for ethene and less selective for coke, while the reverse can be said for particles where tin remains dispersed throughout the particle. This has significant implications for catalyst design, especially given the finding in Sect. 3.2 that surface segregation of tin atoms is less favorable in the presence of adsorbates (hydrogen or carbon atoms) on the surface, which are expected to be present during reaction conditions.

Successive dehydrogenation from methane to carbon on the metal surfaces is depicted in Fig. 5. It was investigated to understand the dehydrogenation for CH_x species after the C–C cleavage of C_2H_x species. The total reaction energies to atomic carbon on Pt, Pt_3Sn/Pt, and Pt_3Sn were 0.45, 1.33, and 1.28 eV, respectively. This suggests that atomic carbon formation from CH_x species would be energetically harder on the alloys than on Pt. Generally, the activation energies also increased when Sn was present and difference became larger. On the alloys, high energy barriers for the dehydrogenation of methylidyne to carbon made carbon formation even more unfavorable. In agreement with our previous work [25], the energetic penalties associated with the formation of atomic carbon on the alloy surfaces make this species unlikely to be a significant contributor to coke formation.

Table 5 Selectivity descriptors for ethane dehydrogenation on all studied surfaces (in eV)

Metric[a]	Pt	Pt_3Sn/Pt	Pt_3Sn
$E_{\mathrm{a,CH2CH2\rightarrow CH2CH}} - \Delta E_{\mathrm{des,CH2CH2}}$[b]	−0.12	0.36	0.04
$E_{\mathrm{a,CH3CH2\rightarrow CH3CH}} - E_{\mathrm{a,CH3CH2\rightarrow CH2CH2}}$	0.07	0.22	−0.03
$\Delta\Delta E = \Delta E_{\mathrm{CH3CH2\rightarrow CH3CH}} - \Delta E_{\mathrm{CH3CH2\rightarrow CH2CH2}}$	0.27	0.26	0.25

[a] $E_{\mathrm{a,i}}$ is the activation energy barrier for the reaction shown, $\Delta E_{\mathrm{des,CH2CH2}}$ is the desorption energy of ethene, ΔE_{i} is the reaction energy for the reaction shown

[b] $\Delta E_{\mathrm{des,CH2CH2}}$ given without entropic contribution. Adding $-T\Delta S$ at 298 K would raise all three values by 0.54 eV, or 1.48 eV at 900 K

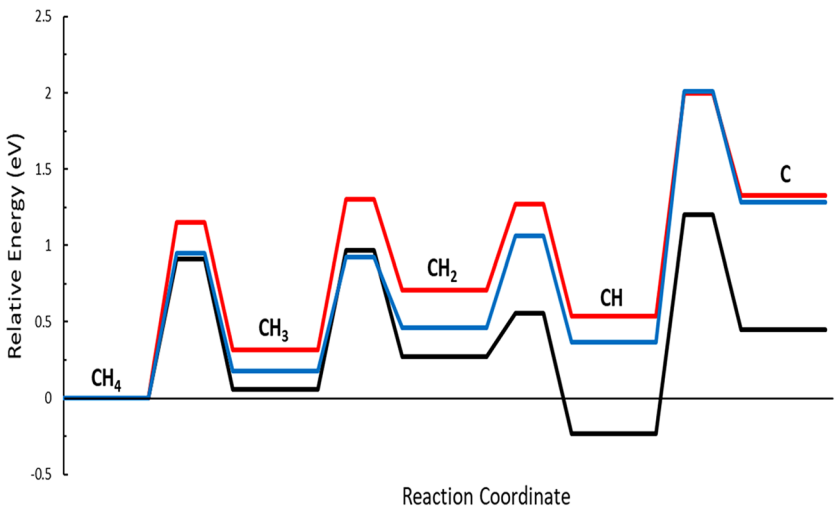

Fig. 5 Potential energy surfaces for successive dehydrogenation of CH_x species from methane to carbon. Black, red, and blue lines indicate the reaction on Pt, Pt_3Sn/Pt, and Pt_3Sn, respectively. All energies are relative to methane on the surface. All species are adsorbed on the surface. Detached hydrogens on the surfaces are omitted for clarity and all species are at infinite separation

3.6 C–C Bond-Breaking Steps in C_2H_x Species

Reaction and activation energies for all elementary reactions for carbon–carbon bond cleavage in C_2H_x species were calculated as summarized in Table 4. In general, C–C bond cleavage was energetically more unfavorable than C–H bond breaking if x was three or larger in C_2H_x species. For example, ethene dehydrogenation to vinyl is energetically uphill on each surface, where the reaction energies are 0.16 eV on Pt, 0.31 eV on Pt_3Sn/Pt, and 0.10 eV on Pt_3Sn. C–C bond breaking of ethene is even more endothermic, where reaction energies are 0.71 eV on Pt, 1.00 eV on Pt_3Sn/Pt, and 0.79 eV on Pt_3Sn. However, with deeper dehydrogenation, C–C bond cleavage of C_2H_x species with x less than three becomes thermodynamically more favorable than C–H bond cleavage. For example, C–H bond breaking of acetylene has reaction energies of 0.94, 1.01, and 0.83 eV on Pt, Pt_3Sn/Pt, and Pt_3Sn, respectively while C–C bond breaking of acetylene has lower reaction energies of − 0.49 eV on Pt, 0.13 eV on Pt_3Sn/Pt, and 0.37 eV Pt_3Sn. The exception is for vinylidene on the alloys, where reaction energies of C–C cleavage are larger than C–H cleavage.

In terms of barriers, C–C cleavage of adsorbates are always harder than C–H cleavage regardless of the surface and degree of dehydrogenation of the reactant C_2H_x species. In Table 4, the energy barriers of C–C bond breaking (1.24–3.42 eV) are significantly higher than the energy barriers of competing C–H bond cleavage (0.25–2.01 eV) for all C_2H_x species on each surface with very few exceptions on pure Pt only. Acetylene and acetylidene on Pt are the only two exceptions, where the energy barriers of C-H bond breaking are 1.69 and 1.71 eV, and C–C bond cleavages are 1.37 and 1.24 eV, respectively.

Sn on the surface increases not only the endothermicity but also the energy barrier of each C–C bond breaking step. In Table 4, the reaction energies of C–C cleavage for all C_2H_x species on Pt_3Sn/Pt are higher than on Pt. Except for two closed-shell species of ethane and ethene, all energy barriers for C–C cleavage on Pt_3Sn/Pt are also higher than on Pt. It implies that Sn on the surface makes C–C cleavage both thermodynamically and kinetically more difficult. On the bulk alloy, the reaction energies for C–C bond breaking are larger than those on Pt for all adsorbates. Compared to the surface alloy, the reaction energies on the bulk alloy are smaller for ethane, ethyl, and ethene that are C_2H_x species on the desirable reaction pathway, comparable for ethylidene, and larger for other C_2H_x species. The activation energies of C–C cleavage on the bulk alloy are higher than those on the surface alloy for many C_2H_x adsorbates. This is especially large for acetylidene such that the difference of activation energy for C–C cleavage between Pt_3Sn/Pt and Pt_3Sn is 1.22 eV. Ethyl, ethylidene, and ethylidyne on Pt_3Sn have the same or lower energy barriers of C–C cleavage than on Pt_3Sn/Pt.

4 Conclusion

DFT calculations were performed to investigate the effect of Sn in the bulk and surface of PtSn alloys on the activity, selectivity, and stability of the catalyst. The comprehensive study including binding energies of all C_xH_y adsorbates, reaction and activation energies for all elementary reactions on Pt, Pt_3Sn/Pt, and Pt_3Sn surfaces was conducted.

The difference in binding energies over the alloys is largely attributed to the electronic interaction changes caused by the strain and/or the ligand effect from *d*-band theory. For the strain effect, tensile strain caused by the larger lattice constant on the bulk alloy made *d*-bands of surface atoms less overlapped followed by *d*-band upshift and less filled anti-bonding orbitals of metal-adsorbate leading to enhance the binding energies of adsorbates. On the other hand, the ligand effect worked in the opposite direction, in that Sn on the surface caused broadening *d*-bands of surface Pt atoms followed by *d*-band downshift leading to more filled anti-bonding states of metal-adsorbate. As a result, binding energies of ethane derivatives were generally in the order of Pt, Pt_3Sn, and Pt_3Sn/Pt.

For reaction energies and energy barriers for all the elementary reactions, Sn promotion on the surface layer generally increased the reaction and activation energies for both C–H and C–C cleavage steps. However, Sn in the bulk did not show this trend. The activity was expected to be highest on Pt, followed by Pt_3Sn and Pt_3Sn/Pt by comparing the energy barriers for ethene formation. The selectivity descriptors were calculated to predict the selectivity toward ethene, which showed that it was favorable on Pt_3Sn/Pt and poor on Pt and Pt_3Sn.

In the present study, we have found the effect of Sn in the bulk is quite different from the effect of Sn in the surface. While increasing tin content in the surface layer may increase selectivity and depress coke formation, adding tin to the bulk of the catalyst does not. Since the addition of adsorbates (hydrogen or carbon) to the surface decreased the surface segregation energy, this may indicate that real catalyst particles become less selective as reaction progresses and tin content in the bulk of the alloy increases.

Acknowledgements This work used resources from the Rutgers Discovery Informatics Institute, which are supported by Rutgers and the State of New Jersey. The authors would like to thank Dr. Alec Hook for his leadership in the early stages of this project.

Funding This work was funded by the National Science Foundation under Grant Number CBET-1705746.

Compliance with Ethical Standards

Conflict of interest The authors declare that they have no conflict of interest.

References

1. Ridha T, Li Y, Gençer E, Siirola JJ, Miller JT, Ribeiro FH, Agrawal R (2018) Processes 6:139
2. Wang Q, Chen X, Jha AN, Rogers H (2014) Renew Sustain Energy Rev 30:1–28
3. Sattler JJHB, Ruiz-Martinez J, Santillan-Jimenez E, Weckhuysen BM (2014) Chem Rev 114:10613–10653
4. Amghizar I, Vandewalle LA, Van Geem KM, Marin GB (2017) Engineering 3:171–178
5. Sadrameli SM (2015) Fuel 140:102–115
6. Cavani F, Ballarini N, Cericola A (2007) Catal Today 127:113–131
7. Sadrameli SM (2016) Fuel 173:285–297
8. Lee DY, Elgowainy A (2018) Int J Hydrog Energy 43:20143–20160
9. Vora BV (2012) Top Catal 55:1297–1308
10. Galvita V, Siddiqi G, Sun P, Bell AT (2010) J Catal 271:209–219
11. Wu J, Peng Z, Bell AT (2014) J Catal 311:161–168
12. Wegener EC, Wu Z, Tseng HT, Gallagher JR, Ren Y, Diaz RE, Ribeiro FH, Miller JT (2018) Catal Today 299:146–153
13. Siddiqi G, Sun P, Galvita V, Bell AT (2010) J Catal 274:200–206
14. Xiao L, Ma F, Zhu YA, Sui ZJ, Zhou JH, Zhou XG, Chen D, Yuan WK (2019) Chem Eng J 377:120049
15. Yang ML, Zhu YA, Zhou XG, Sui ZJ, Chen D (2012) ACS Catal 2:1247–1258
16. Nykänen L, Honkala K (2011) J Phys Chem C 115:9578–9586
17. Nykänen L, Honkala K (2013) ACS Catal 3:3026–3030
18. Hansen MH, Nørskov JK, Bligaard T (2019) J Catal 374:161–170
19. Zhang Y, Zhou Y, Shi J, Zhou S, Sheng X, Zhang Z, Xiang S (2014) J Mol Catal A 381:138–147
20. Lee MH, Nagaraja BM, Lee KY, Jung KD (2014) Catal Today 232:53–62
21. Kim J, Fu J, Podkolzin SG, Koel BE (2010) J Phys Chem C 114:17238–17247
22. Liu Y, Li D, Stamenkovic VR, Soled S, Henao JD, Sun S (2011) ACS Catal 1:1719–1723
23. Somodi F, Peng Z, Getsoian AB, Bell AT (2011) J Phys Chem C 115:19084–19090
24. Crabb EM, Marshall R, Thompsett D (2000) J Electrochem Soc 147:4440–4447
25. Hook A, Massa JD, Celik FE (2016) J Phys Chem C 120:27307–27318
26. Chen Y, Vlachos DG (2010) J Phys Chem C 114:4973–4982
27. Yang ML, Zhu J, Zhu YA, Sui ZJ, Yu YD, Zhou XG, Chen D (2014) J Mol Catal A 395:329–336
28. Haubrich J, Becker C, Wandelt K (2009) Surf Sci 603:1476–1485
29. Peng G, Gerceker D, Kumbhalkar M, Dumesic JA, Mavrikakis M (2018) Catal Sci Technol 8:2159–2174
30. Hook A, Celik FE (2017) J Phys Chem C 121:17882–17892
31. Saerens S, Sabbe MK, Galvita VV, Redekop EA, Reyniers MF, Marin GB (2017) ACS Catal 7:7495–7508
32. Kresse G, Furthmüller J (1996) Comput Mater Sci 6:15–50
33. Kresse G, Furthmüller J (1996) Phys Rev B 54:11169–11186
34. Perdew JP, Wang Y (1992) Phys Rev B 45:13244–13249
35. Blöchl PE (1994) Phys Rev B 50:17953–17979
36. Kresse G, Joubert D (1999) Phys Rev B 59:1758–1775
37. Jiang L, Sun G, Sun S, Liu J, Tang S, Li H, Zhou B, Xin Q (2005) Electrochim Acta 50:5384–5389
38. Atrei A, Bardi U, Rovida G, Torrini M, Zanazzi E (1992) Phys Rev B 46:1649–1654
39. Neugebauer J, Scheffler M (1992) Phys Rev B 46:16067–16080
40. Monkhorst HJ, Pack JD (1976) Phys Rev B 13:5188–5192
41. Henkelman G, Uberuaga BP, Jónsson H (2000) J Chem Phys 113:9901–9904
42. Duan Z, Zhong J, Wang G (2010) J Chem Phys 133:114701
43. Viñes F, Lykhach Y, Staudt T, Lorenz MPA, Papp C, Steinrück HP, Libuda J, Neyman KM, Görling A (2010) Chem Eur J 16:6530–6539
44. Yang ML, Zhu YA, Fan C, Sui ZJ, Chen D, Zhou XG (2010) J Mol Catal A 321:42–49
45. Watwe RM, Cortright RD, Mavrikakis M, Nørskov JK, Dumesic JA (2001) J Chem Phys 114:4663–4668
46. Zhao ZJ, Moskaleva LV, Aleksandrov HA, Basaran D, Rösch N (2010) J Phys Chem C 114:12190–12201
47. Hammer B, Nørskov JK (1995) Surf Sci 343:211–220
48. Hammer B, Nørskov JK (1995) Nature 376:238–240
49. Xu Y, Ruban AV, Mavrikakis M (2004) J Am Chem Soc 126:4717–4725
50. Delbecq F, Sautet P (2003) J Catal 220:115–126
51. Kitchin JR, Nørskov JK, Barteau MA, Chen JG (2004) J Chem Phys 120:10240–10246
52. Tasbihi M, Feyzi F, Amlashi MA, Abdullah AZ, Mohamed AR (2007) Fuel Process Technol 88:883–889